

## Hydrogen embrittlement of high strength steam turbine last stage blade steels: Comparison between PH17-4 steel and PH13-8Mo steel

Xinfeng Li<sup>a,b,\*</sup>, Jin Zhang<sup>c</sup>, Qinqin Fu<sup>b</sup>, Eiji Akiyama<sup>d</sup>, Xiaolong Song<sup>b</sup>, Sicong Shen<sup>b</sup>, Qizhen Li<sup>a,\*\*</sup>

<sup>a</sup> School of Mechanical and Materials Engineering, Washington State University, Pullman 99164, USA

<sup>b</sup> State Key Laboratory for Mechanical Behavior of Materials, Xi'an Jiaotong University, Xi'an 710049, China

<sup>c</sup> Department of Physics and Astronomy, Washington State University, Pullman 99164, USA

<sup>d</sup> Institute for Materials Research, Materials Design Division, Tohoku University, Sendai 980-8577, Japan



### ARTICLE INFO

#### Keywords:

Hydrogen embrittlement  
Hydrogen diffusion behaviors  
Precipitation-hardening martensitic steels  
Slow strain rate tensile tests

### ABSTRACT

Hydrogen embrittlement behaviors of PH17-4 steel and PH13-8Mo steel used as steam turbine last stage blades were investigated by means of slow strain rate tensile tests and hydrogen permeation tests. The results indicate that PH13-8Mo steel exhibits higher strength level mainly due to higher precipitate strengthening and lath strengthening compared with PH17-4 steel in the absence of hydrogen. Moreover, pre-hydrogen charging does not affect tensile strength of PH17-4 steel, but decreases tensile strength of PH13-8Mo steel. The plasticity of PH17-4 steel and PH13-8Mo steel is degraded after hydrogen charging and the deterioration is accompanied with considerable change in fracture mode. The loss of plasticity of PH13-8Mo steel is higher than that of PH17-4 steel, indicating that PH13-8Mo steel exhibits lower resistance to hydrogen embrittlement, which is mainly related to higher hydrogen diffusion behaviors and higher strength level of PH13-8Mo steel. Additionally, PH17-4 steel exhibits lower apparent hydrogen diffusion coefficient and higher apparent hydrogen solubility in comparison with those of PH13-8Mo steel, which implies that incoherent Cu-rich precipitates in PH17-4 steel possess higher capability to trap hydrogen atoms than that of coherent NiAl precipitates in PH13-8Mo steel.

### 1. Introduction

In 1940s, precipitation-hardening (PH) martensitic steels were firstly developed. These alloys were added some elements, such as Mo, Cu, Nb, Ti, to increase strength level on the basis of chemical compositions of Cr13 type martensitic steels. Among PH steels, representative steels are PH17-4 steel and PH13-8Mo steel [1]. The addition of approximate 3% Cu in weight for PH17-4 steel and 1% Al in weight for PH13-8Mo steel is conducted to form nano-sized Cu-rich precipitates or NiAl precipitates within martensitic matrix during ageing treatments [1–3] so that the alloys exhibit high strength level. Meanwhile, austenite stabilizing elements such as Ni would segregate at localized defect sites, resulting in the formation of reversed austenite [4]. The existence of reversed austenite causes relatively good plasticity as well as excellent corrosion resistance for steels. Accordingly, both steels usually serve as key structural materials used in aerospace, aircraft and nuclear industries [1,5,6].

In the power plants, PH17-4 steel and PH13-8Mo steel are widely used to manufacture steam turbine last stage blades, as shown in Fig. 1.

However, premature failures of the blades frequently occur, leading to steam turbine vibration, work efficiency reduction, even whole steam turbines destroy with huge economic loss and casualties [7,8]. According to the statistics report from the Electric Power Research Institute, economic loss due to power plant downtime caused by blade failures had been about 15.5–18.4 billion dollars from 1977 to 1981 [9]. Post-mortem failure analysis results indicate that hydrogen-related cracking has played an important role in failures of steam turbine blades [10–18]. Further, corrosion reactions take place on the blade surfaces during their service and hydrogen atoms are generated through partial cathodic reaction ( $H^+ + e^- \rightarrow H(\text{atom})$ ) to some extent [19,20]. Hereafter, hydrogen atoms would diffuse into the interior of the alloys and interact with microstructures of the alloys, which results in failure of the alloys due to hydrogen embrittlement (HE). In addition, PH17-4 steel and PH13-8Mo steel possess high strength level up to 1400 MPa. As reported in previous studies [2,21], high strength of the steels correlates with low resistance to HE. Hence, more and more attention has been paid to HE behaviors of PH17-4 steel [22–25] and PH13-8Mo steel [2,5,21,26–28], respectively. However, the comparison

\* Corresponding author at: School of Mechanical and Materials Engineering, Washington State University, Pullman 99164, USA.

\*\* Corresponding author.

E-mail addresses: [xinfeng.li@wsu.edu](mailto:xinfeng.li@wsu.edu), [xinfengli0718@gmail.com](mailto:xinfengli0718@gmail.com) (X. Li), [qizhen.li@wsu.edu](mailto:qizhen.li@wsu.edu) (Q. Li).

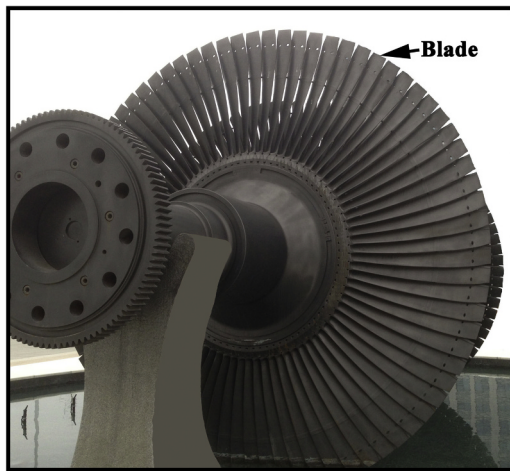


Fig. 1. Steam turbine blades manufactured from precipitation-hardening martensitic steels.

of HE behaviors between high strength PH17-4 and PH13-8Mo steam turbine blade steels has not yet been reported.

In the present study, tensile samples were directly cut from PH17-4 and PH13-8Mo blade steels and tensioned at low strain rate to investigate their HE behaviors. Then, the role of microstructure of the alloys on hydrogen diffusion behaviors and resistance to HE was discussed.

## 2. Experimental procedures

### 2.1. Materials preparation

The materials used in this study were PH17-4 and PH13-8Mo martensitic stainless steels and corresponding nominal chemical compositions of the steels are listed in Table 1.

PH17-4 steel bars were solution-treated at 1040 °C for 1 h, quenched in the oil to the room temperature, aged at 480 °C for 3 h and then air-cooled. Meanwhile, solution temperature of PH13-8Mo steel bars was 925 °C for 1 h. Then the samples were quenched in the oil and aged at 540 °C for 4 h, followed by cooling in air. Fig. 2 shows corresponding schematic diagram of heat treatment processes of the steels.

The different heat treatment processes of two steels were selected to be in accordance with practical heat treatments of the turbine blades, by which peak strength of two steels was obtained [22,28].

### 2.2. Microstructural characterization

Following standard grinding and polishing procedures, metallographic specimens were etched in the solution, which was composed of 200 ml hydrochloric acid and 1000 ml deionized water with 100 g ferric trichloride, and observed under optical microscopy (OM) (Zeiss Axio Scope, Thornwood, NY) and scanning electron microscopy (SEM) (FEI Quanta 200 F, Hillsboro, OR). To further study the sub-microstructures of the alloys, high resolution transmission electron microscopy (HRTEM) (JEOL 2100 F, Akishima-shi, Kyoto) operated at 200 kV was used to characterize martensitic lath and precipitates. The thin foils for HRTEM observation were prepared using a twin-jet electro-polishing apparatus in the solution containing 10% (vol.) perchloric acid and

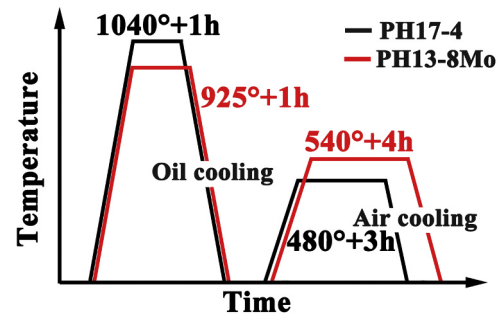


Fig. 2. Schematic diagram of heat treatment conditions for PH17-4 steel (black lines) and PH13-8Mo steel (red lines).

90% (vol.) ethanol at  $-30$  °C. This constant temperature was maintained by adding liquid nitrogen. The voltage for twin-jet electro-polishing tests was about 20 V. In addition, X-rays diffraction (XRD) (XRD-7000, Shimadzu, Kyoto) using a  $\text{Cu K}\alpha$  radiation operated at 40 kV was used to detect the content of retained/reversed austenite in the steels. The scanning range was from  $40^\circ$  to  $95^\circ$  with a scanning rate of  $5^\circ \text{min}^{-1}$  and a step size of  $0.02^\circ$  respectively.

### 2.3. The evaluation of hydrogen embrittlement susceptibility

Smooth cylindrical tensile samples with a diameter of 5 mm and a gauge length of 25 mm (Fig. 3) were prepared from the steel bars. These tensile samples were divided into two groups. One group was free of hydrogen charging (HF) and the other group was subjected to electrochemical pre-hydrogen charging (HC). Hydrogen charging tests were conducted in a 0.5 M  $\text{H}_2\text{SO}_4$  solution with  $1 \text{ g L}^{-1}$  thiourea at  $0.06 \text{ mA cm}^{-2}$  for 24 h. The selection of hydrogen charging current density and time was consistent with previous experimental parameters [2,5] and the addition of thiourea was to increase hydrogen entry [29]. To evaluate hydrogen-assisted degradation on mechanical properties of the steels, slow strain rate tensile (SSRT) tests were carried out on both HF samples and HC samples at a constant crosshead speed of  $0.03 \text{ mm min}^{-1}$ , which was equivalent to a nominal strain rate of  $2 \times 10^{-5} \text{ s}^{-1}$ , using a screw-driven uniaxial tensile machine (Instron 1195, Norwood, MA). The tensile strain rate was consistent with ASTM G129-00 standard. After SSRT tests, the index of relative sensibility to HE (HEI) was determined by measuring relative plasticity loss, which was expressed as [30–32]:

$$\varphi - \text{loss} = \frac{\varphi_{(\text{HF})} - \varphi_{(\text{HC})}}{\varphi_{(\text{HF})}} \times 100\% \quad (1)$$

$$\varepsilon_f - \text{loss} = \frac{\varepsilon_{f(\text{HF})} - \varepsilon_{f(\text{HC})}}{\varepsilon_{f(\text{HF})}} \times 100\% \quad (2)$$

where  $\varphi_{(\text{HF})}$  and  $\varepsilon_{f(\text{HF})}$  were the reduction of area and the fracture strain of HF specimens, whereas  $\varphi_{(\text{HC})}$  and  $\varepsilon_{f(\text{HC})}$  were the reduction of area and the fracture strain of HC specimens, respectively.

### 2.4. Hydrogen permeation tests

Hydrogen permeation behaviors of the steels were investigated using modified Devanathan-Stachursky devices [33]. The sheet samples were clamped between two cells, where one surface of the samples served as hydrogen entry side and the other acted as hydrogen exit side.

Table 1

Chemical compositions of PH17-4 steel and PH13-8Mo steel in this study (wt%).

	C	Si	Mn	Cr	Ni	Cu	Nb	Al	N	Mo	Fe
PH17-4 [22]	0.01	0.82	0.48	16.14	4.07	3.15	0.26	–	–	–	Balance
PH13-8Mo	0.03	0.05	0.10	12.50	8.00	–	–	1.12	0.003	2.30	Balance

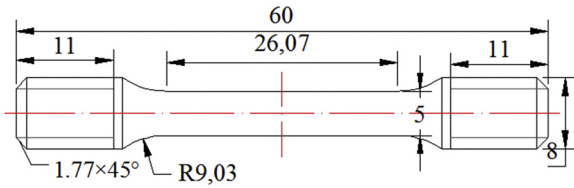


Fig. 3. Dimensions of a tensile specimen (in mm) [2].

Hydrogen entry side was galvanostatically polarized at a constant current density of  $20 \text{ mA cm}^{-2}$  in  $0.5 \text{ M H}_2\text{SO}_4$  solution with  $1 \text{ g L}^{-1}$  thiourea. Meanwhile, hydrogen exit side was potentiostatically maintained at a constant potential of  $0.2 \text{ V}$  versus reference electrode (Hg/HgO/NaOH  $0.1 \text{ M NaOH}$ ). Note that the residual hydrogen in the samples was depleted until the current was below  $1 \mu\text{A}$  before hydrogen charging.

During hydrogen permeation tests, Fick's law can be used to determine hydrogen diffusion behaviors in the samples as:

$$J = -D \frac{\partial C}{\partial x}, \quad \frac{\partial C}{\partial t} = D \frac{\partial^2 C}{\partial x^2} \quad (3)$$

where  $J$  was diffusion flux,  $D$  was hydrogen diffusion coefficient.  $C$  was hydrogen concentration,  $x$  was the distance from the sample surface,  $t$  was hydrogen charging time. At hydrogen entry side, a constant hydrogen concentration ( $C_0$ ) can be obtained because of fixed hydrogen charging current density, whereas applied constant potential made hydrogen atoms to be immediately oxidized to hydrogen ions so that hydrogen concentration at exit side was zero. That is to say, corresponding boundary conditions of samples during hydrogen permeation tests were expressed as:

$$C(x, t = 0) = 0, \quad C(0, t) = C_0, \quad C(l, t) = 0 \quad (4)$$

where  $l$  was the thickness of the sample. Using the solution, hydrogen permeability coefficient ( $J_\infty l$ ), apparent hydrogen diffusion coefficient ( $D_{app}$ ) can be obtained by [20]:

$$J_\infty l = \frac{I_P^\infty l}{nF} \quad (5)$$

$$D_{app} = \frac{l^2}{6t_L} \quad (6)$$

where  $I_P^\infty$  was the steady-state permeation current density,  $n$  was the number of electrons transferred,  $F$  was the Faraday's constant,  $t_L$  was the lag time, defined as 0.63 times the steady-state value, as shown in Fig. 4. Apparent hydrogen solubility near sample surface ( $C_{app}$ ) was calculated by [22]:

$$C_{app} = \frac{J_\infty l}{D_{app}} \quad (7)$$

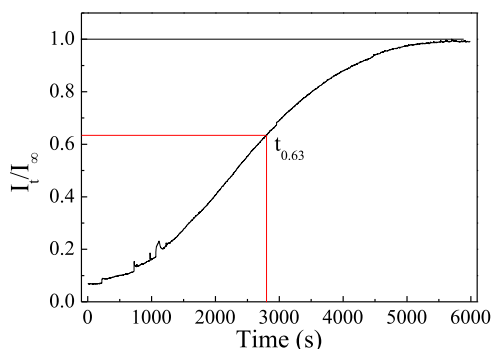


Fig. 4. Schematic diagram of hydrogen permeation curve showing calculating lag time.

### 3. Results

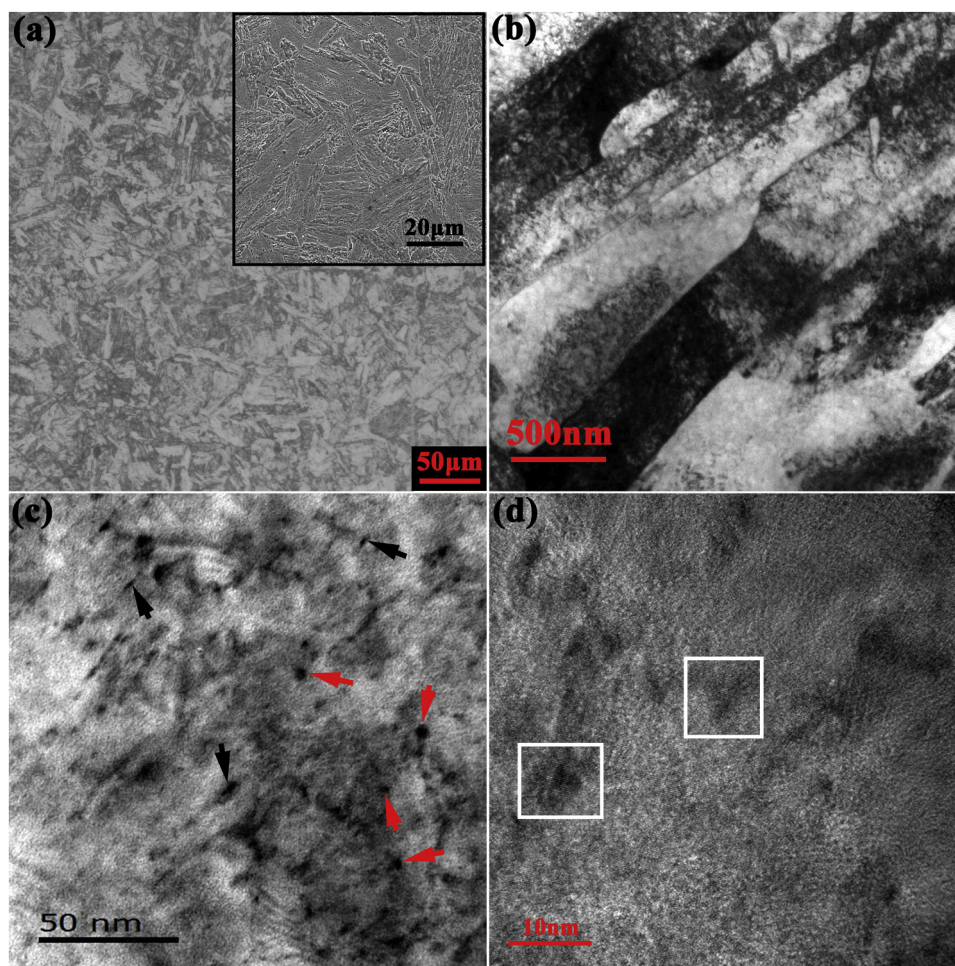
#### 3.1. Microstructural characteristics

Fig. 5 and Fig. 6 show OM, SEM and TEM microstructure images of the tested PH17-4 steel and PH13-8Mo steel, respectively. Both PH17-4 steel and PH13-8Mo steel exhibit fully martensitic microstructures, as shown in Fig. 5(a) and Fig. 6(a). TEM observation further reveals that sub-microstructures of the steels consist of a typical lath martensite with a number of dislocations (Fig. 5(b) and Fig. 6(b)). However, it is worth noting that precipitates in the steels are different. For PH17-4 steel, spherical-shape (indicated by red arrows) and elliptical-shape (indicated by black arrows) Cu-rich precipitates demonstrated in previous study [22] are observed (Fig. 5(c)), and HRTEM image indicates that Cu-rich precipitates are not well-bonded with the matrix (Fig. 5(d)), which is consistent with results from Hsiao et al. [34]. The value of the interplanar spacing is  $0.201 \text{ nm}$ , which corresponds to the spacing of (111) planes in FCC Cu ( $0.208 \text{ nm}$ ) with  $Fm-3m$  space group. Additionally, Fig. 6(c) shows NiAl precipitates in PH13-8Mo steel, as confirmed by selected area electron diffraction (SAED) (Fig. 6(e)), where weak spots are identified as [100] from NiAl phase. According to the diffraction pattern, NiAl precipitate has a BCC structure and crystal orientation relationship between the precipitates with the matrix is  $(110)_\alpha // (110)_{\text{NiAl}}$ . Fig. 6(d) presents corresponding HRTEM image of NiAl precipitates, revealing that no sharp interfaces between the matrix and NiAl precipitates are observed, i.e., NiAl precipitates are highly coherent with the matrix. A study [35] reports that NiAl precipitates are resistant to coarsening and keep coherency with the matrix, even at  $620 \text{ }^\circ\text{C}$  for 4 h.

Fig. 7 presents histograms of grain size, lath spacing and precipitate size of PH17-4 steel and PH13-8Mo steel, and these histograms basically obey normal distributions. The grain size and lath spacing histograms of PH17-4 steel show wide distributions, whereas they presents narrow distributions for PH13-8Mo steel. Further, average grain size, lath size and precipitate size, which were defined as the total sizes divided by the total numbers, are  $27 \mu\text{m}$ ,  $250 \text{ nm}$  and  $3.84 \text{ nm}$  for PH17-4 steel and  $23 \mu\text{m}$ ,  $212 \text{ nm}$  and  $3.25 \text{ nm}$  for PH13-8Mo steel respectively. It is concluded that average grain size and lath size in PH17-4 steel are slightly larger than those of PH13-8Mo steel, which is related to higher solution temperature of PH17-4 steel compared with that of PH13-8Mo steel ( $1040 \text{ }^\circ\text{C}$  against  $925 \text{ }^\circ\text{C}$ ). Additionally, it is well-established that the precipitation of Cu-rich precipitates in PH17-4 steel or NiAl precipitates in PH13-8Mo steel takes place during ageing treatment, and the nucleation and growth of these precipitates refer to a diffusion process [4,26,36]. The diffusion coefficient of Ni and Al in  $\alpha$ -iron matrix at  $540 \text{ }^\circ\text{C}$  is approximate  $3.2 \times 10^{-20} \text{ m}^2 \text{ s}^{-1}$  [37] and  $3.1 \times 10^{-25} \text{ m}^2 \text{ s}^{-1}$  [38] respectively, whereas it is about  $5.4 \times 10^{-22} \text{ m}^2 \text{ s}^{-1}$  for Cu in  $\alpha$ -iron matrix at  $480 \text{ }^\circ\text{C}$  [39]. Due to low diffusion coefficient of Al in  $\alpha$ -iron matrix, NiAl precipitates in PH13-8Mo steel exhibit higher resistance to nucleation and growth accompanied with smaller average size ( $3.25 \text{ nm}$ ) in comparison with that of Cu-rich precipitates in PH17-4 steel ( $3.84 \text{ nm}$ ). Fig. 8 shows XRD patterns of both steels, indicating that retained/reversed austenite was absent for PH17-4 steel and PH13-8Mo steel. This result is in accordance with previous studies [2,22].

#### 3.2. Hydrogen embrittlement behaviors

Typical tensile stress versus strain curves of HF and HC samples are shown in Fig. 9 and corresponding mechanical properties of the steels are summarized in Table 2. Both steels without hydrogen charging exhibit superior mechanical properties, i.e., yield strength, tensile strength, fracture strain and reduction of area are  $1293 \text{ MPa}$ ,  $1430 \text{ MPa}$ ,  $13.75\%$  and  $58.53\%$  for PH17-4 sample, and  $1435 \text{ MPa}$ ,  $1495 \text{ MPa}$ ,  $12.53\%$  and  $56.09\%$  for PH13-8Mo sample, respectively. In comparison with PH17-4 steel, PH13-8Mo steel shows an increase of  $142 \text{ MPa}$  in yield strength,  $65 \text{ MPa}$  in tensile strength, but a little decrease in



**Fig. 5.** Microstructures of PH17-4 steel sample (a) optical microstructure; (b) lath martensite; (c) Cu-rich precipitates; (d) high magnification image of Cu-rich precipitates. Red arrows indicating spherical-shape precipitates; Black arrows showing elliptical-shape precipitates; White rectangles indicating incoherent Cu-rich precipitates.

fracture strain (1.22%) and reduction of area (2.44%). The higher strength of PH13-8Mo steel is attributed to its smaller coherent NiAl precipitates with low lattice misfit, which needs high cutting stress to separate precipitates from the matrix [40], and its smaller grain sizes of matrix based on Hall-Petch relation [41]. After hydrogen charging, yield strength and tensile strength of PH17-4 steel do not change, whereas fracture strain decreases to 3.57%. In contrast, hydrogen-assisted fracture failure of PH13-8Mo steel occurs at the elastic stage with tensile strength of 1185 MPa and fracture strain of 0.56%. Moreover, the values of both  $\varphi - loss$  (88.93%) and  $\varepsilon_f - loss$  (74.04%) for PH17-4 steel are lower than those of PH13-8Mo steel (98.56% and 95.53%), implying that the resistance to HE of PH17-4 steel is higher than that of PH13-8Mo steel.

The parameters of hydrogen diffusion behaviors of both steels are listed in Table 3. The values of  $J_{\infty l}$  and  $D_{app}$  of PH17-4 steel are lower than those of PH13-8Mo steel, that is to say, from  $2.69 \times 10^{-9} \text{ mol m}^{-1} \text{ s}^{-1}$  to  $5.28 \times 10^{-9} \text{ mol m}^{-1} \text{ s}^{-1}$  and from  $2.18 \times 10^{-12} \text{ m}^2 \text{ s}^{-1}$  to  $9.42 \times 10^{-12} \text{ m}^2 \text{ s}^{-1}$ , while PH17-4 steel exhibits higher value of  $C_{app}$  ( $1235 \text{ mol m}^{-3}$ ) than that of PH13-8Mo steel ( $561 \text{ mol m}^{-3}$ ). Thus, it is implied that PH13-8Mo steel is more permeable to hydrogen atoms than PH17-4 steel. Combining with the susceptibility to HE of the steels, we can obtain that low hydrogen diffusivity and high hydrogen solubility in PH17-4 steel correlate with its low HE sensibility.

### 3.3. Fracture surface observation

Fracture surfaces of PH17-4 and PH13-8Mo samples without and with hydrogen charging are shown in Fig. 10. In the absence of hydrogen, fracture surfaces of both steels are composed of dimples with a variety of sizes (Fig. 10(a) and (c)). Careful observation indicates the depth and diameter of dimples of PH17-4 steel are smaller than those of PH13-8Mo steel. However, several large and deep secondary cracks indicated by white arrows in Fig. 10(a) exist in PH17-4 steel, whereas PH13-8Mo steel presents relatively small secondary cracks indicated by white arrows in Fig. 10(c). These cracks can absorb energy, relief stress concentration and reduce main crack propagation rate [41], resulting in higher plasticity in PH17-4 steel, although PH13-8Mo steel has larger and deeper dimples. After hydrogen charging, fracture surfaces of PH17-4 steel and PH13-8Mo steel are brittle. Only quasi-cleavage fracture feature is detected in PH17-4 steel (Fig. 10(b)) and PH13-8Mo steel shows the coexistence of quasi-cleavage fracture and intergranular fracture (Fig. 10(d)). According to previous studies [42–44], hydrogen-related quasi-cleavage fracture can be explained by a “glide plane decohesion” mechanism. This mechanism has assumed that dislocation mobility increases along particular glide planes in the presence of hydrogen, resulting in localization of hydrogen concentration in these planes due to hydrogen transport by dislocation and stress-induced hydrogen accumulation. Subsequently, locally accumulated hydrogen lowers the cohesion of these planes and quasi-cleavage fracture occurs. Further, it has been demonstrated that these specific glide planes in

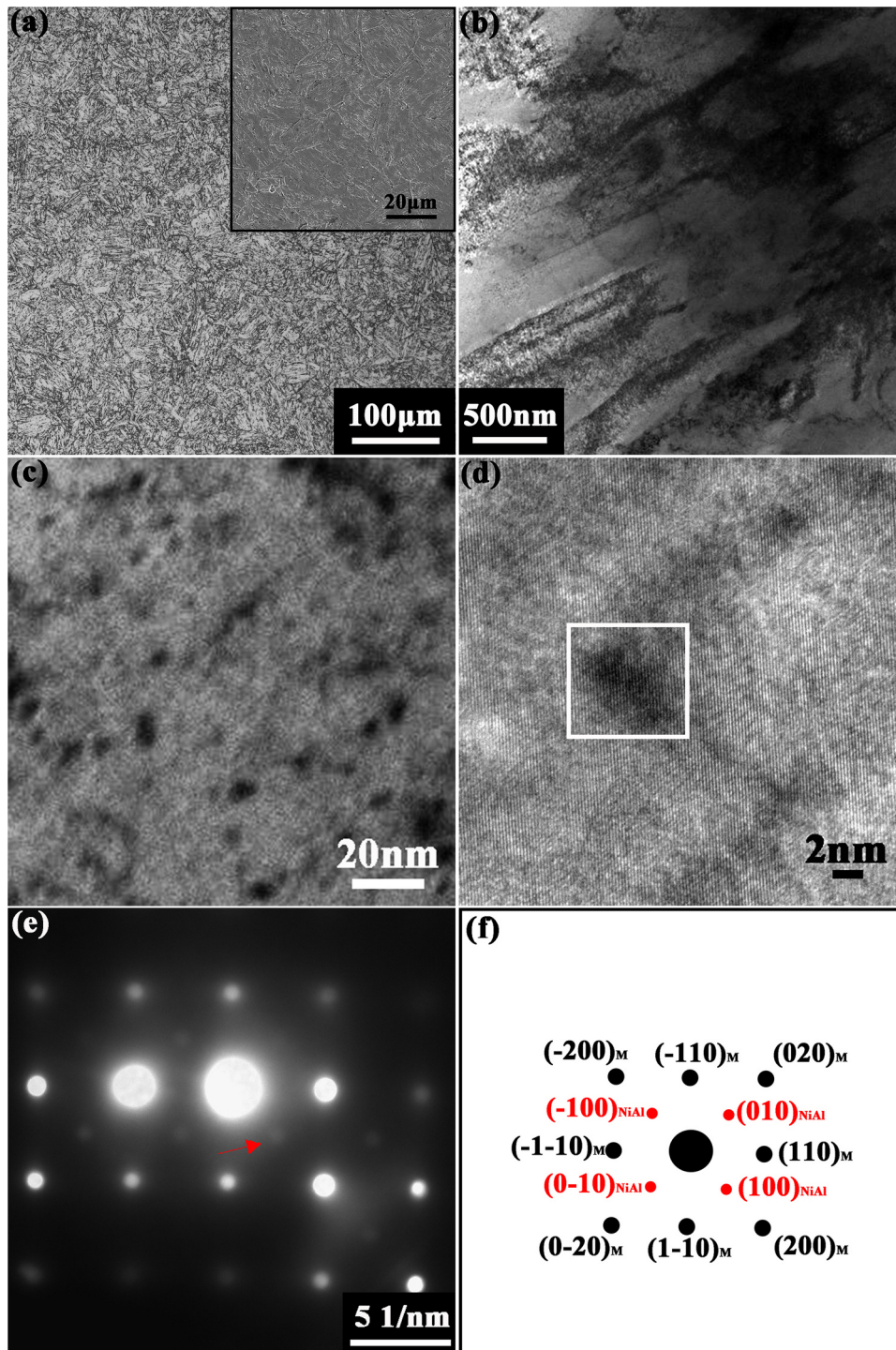


Fig. 6. Microstructures of PH13-8Mo steel sample (a) optical microstructure; (b) lath martensite; (c) NiAl precipitates; (d) high magnification image of NiAl precipitates; (e) and (f) selected area electron diffraction. White rectangle indicating coherent NiAl precipitates.

BCC iron are {110} and {112} planes [45]. In contrast, hydrogen-assisted intergranular fracture of martensitic steels is related to prior austenite grain boundary decohesion because of hydrogen segregation along grain boundaries [46]. After hydrogen charging, fracture mode can transit from dimple fracture, to quasi-cleavage fracture, to cleavage, to intergranular fracture or mixed fracture. Simultaneously, the change of fracture mode accompanies with increasing HE sensibility [26,47]. Hence, mixed quasi-cleavage fracture and intergranular fracture are believed to be the evidence of lower resistance to HE of PH13-8Mo steel compared with PH17-4 steel.

Fig. 11 presents lateral side images of fractured samples of PH17-4 and PH13-8Mo steels. As shown in Fig. 11(a) and Fig. 11(c), severe necking deformation of HF samples is observed for both steels. Corresponding high magnification images of necking zones are shown in Fig. 11(a') and Fig. 11(c'), indicating that there are a number of plastic deformation bands. In contrast, fracture surface of HC PH17-4 steel shows the certain degree of necking, as shown in Fig. 11(b), with slight deformation bands, as seen from Fig. 11(b'). Furthermore, several micro-cracks are detected and magnified micro-crack image is presented in lower right corner in Fig. 11(b). It can be seen that micro-

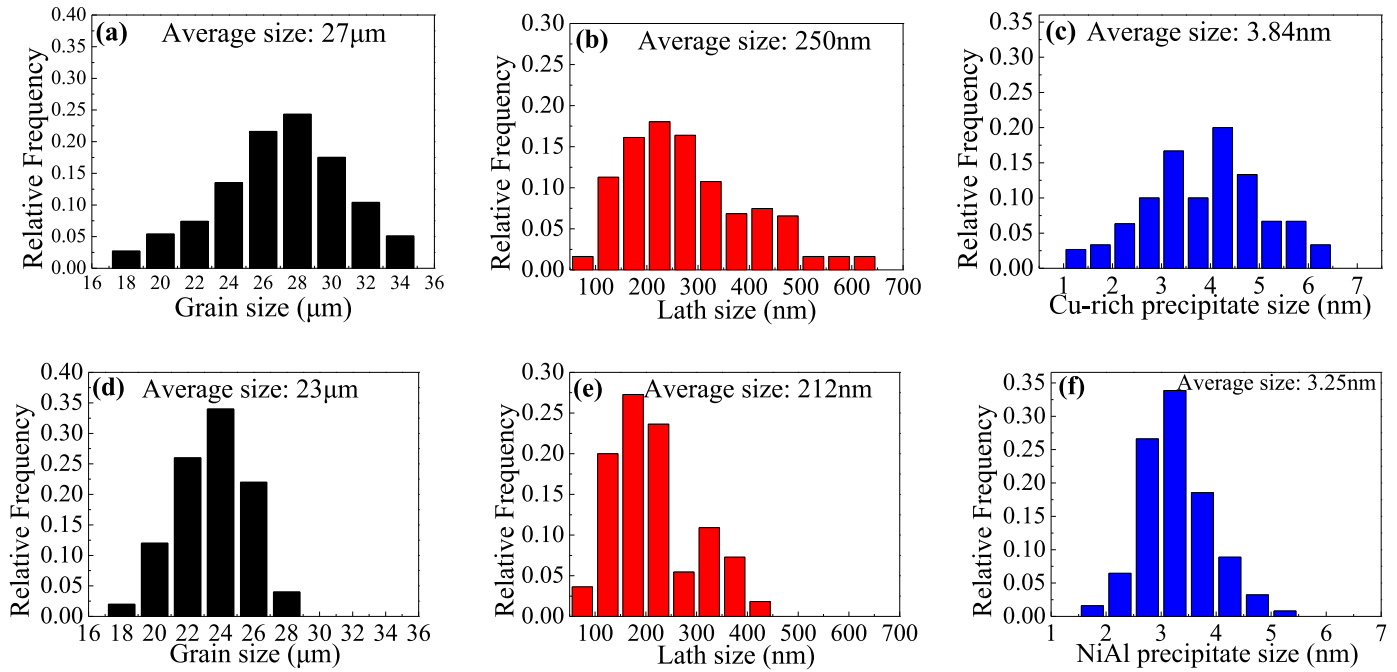


Fig. 7. Histograms of grain size, lath size and precipitate size (a), (b) and (c) PH17-4 steel; (d), (e) and (f) PH13-8Mo steel.

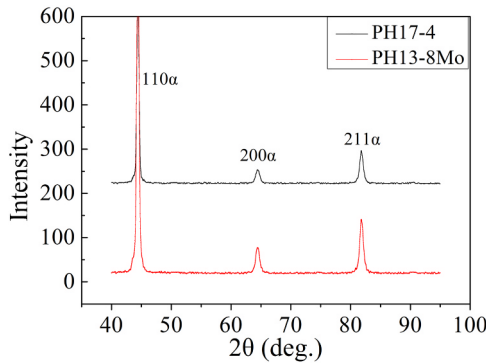


Fig. 8. X-ray diffraction patterns of PH17-4 steel (black line) and PH13-8Mo steel (red line).

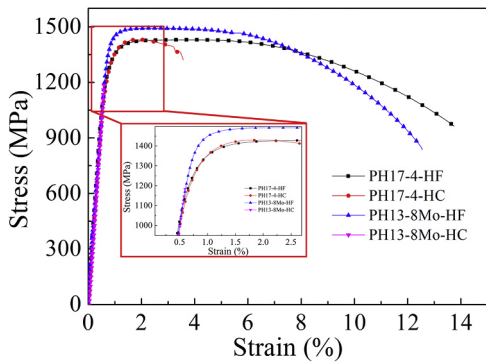


Fig. 9. Tensile stress-strain curves of PH17-4 steel and PH13-8Mo steel with and without hydrogen. HF: hydrogen free. HC: hydrogen charged.

crack propagation direction is approximately perpendicular to tensile direction, which is related with the maximum normal stress [2]. Fig. 11(d) presents fracture surface of HC PH13-8Mo steel and it is also

brittle fracture. Corresponding high magnification image implies a relatively smooth surface with crossed scratches, as shown in Fig. 11(d').

#### 4. Discussion

##### 4.1. Hydrogen diffusion behaviors of PH17-4 steel and PH13-8Mo steel

Hydrogen permeation test results indicate that PH17-4 steel exhibits lower  $D_{app}$  and higher  $C_{app}$  in comparison with those of PH13-8Mo steel ( $2.18 \times 10^{-12} \text{ m}^2 \text{ s}^{-1}$  against  $9.42 \times 10^{-12} \text{ m}^2 \text{ s}^{-1}$  for  $D_{app}$  and  $1235 \text{ mol m}^{-3}$  versus  $561 \text{ mol m}^{-3}$  for  $C_{app}$ ). The difference of hydrogen diffusion behaviors in both steels correlates with hydrogen trapping sites of the steels [48–50]. During hydrogen permeation tests, hydrogen atoms at hydrogen entry side diffuse towards hydrogen exit side under hydrogen concentration gradient after hydrogen trapping sites near hydrogen entry side are filled with hydrogen atoms. Therefore, an increase in the number of effective trapping sites in the alloys can decrease hydrogen diffusivity and increase hydrogen solubility. For PH17-4 steel and PH13-8Mo steel, hydrogen trapping sites contains interstitial, dislocations, lath boundaries, grain boundaries, Cu-rich precipitates [16,21,51] or NiAl precipitates [35]. In this study, the effect of different hydrogen trapping sites on  $D_{app}$  of the alloys is hypothetically summarized as [52]:

$$D_{app} = D_{interstitial} + D_{dislocations} + D_{lath\ boundaries} + D_{grain\ boundaries} + D_{precipitates} \quad (8)$$

where  $D_{interstitial}$ ,  $D_{dislocations}$ ,  $D_{lath\ boundaries}$ ,  $D_{grain\ boundaries}$  and  $D_{precipitates}$  are the contribution of interstitial, dislocations, lath boundaries, grain boundaries and precipitates traps on  $D_{app}$ . Noting that with an increase in effective hydrogen traps, hydrogen diffusion coefficient decreases.

For PH17-4 steel, the Eq. (8) can be written as:

$$D_{app}(PH17-4) = D_{interstitial}(PH17-4) + D_{dislocations}(PH17-4) + D_{lath\ boundaries}(PH17-4) + D_{grain\ boundaries}(PH17-4) + D_{precipitates}(PH17-4) \quad (9)$$

And for PH13-8Mo steel, it can be described as:

**Table 2**  
Mechanical properties of hydrogen free (HF) and hydrogen charged (HC) PH17-4 and PH13-8Mo samples.

	Yield strength (MPa)	Tensile strength (MPa)	Fracture strain (%)	Reduction of area (%)	$\varphi - loss \%$	$\varepsilon_f - loss \%$
PH17-4-HF [22]	1293	1430	13.75	58.53	88.93	74.04
PH17-4-HC [22]	1294	1430	3.57	6.48		
PH13-8Mo-HF	1435	1495	12.53	56.09	98.56	95.53
PH13-8Mo-HC	–	1185	0.56	0.80		

**Table 3**  
Hydrogen permeation test results of PH17-4 and PH13-8Mo samples.

	$J_{\infty}l$ (mol m <sup>-1</sup> s <sup>-1</sup> )	$D_{app}$ (m <sup>2</sup> s <sup>-1</sup> )	$C_{app}$ (mol m <sup>-3</sup> )
PH17-4 [22]	$2.69 \times 10^{-9}$	$2.18 \times 10^{-12}$	1235
PH13-8Mo	$5.28 \times 10^{-9}$	$9.42 \times 10^{-12}$	561

$$D_{app}(PH13-8) = D_{interstitial}(PH13-8) + D_{dislocations}(PH13-8) + D_{lath\ boundaries}(PH13-8) + D_{grain\ boundaries}(PH13-8) + D_{precipitates}(PH13-8) \tag{10}$$

Because PH17-4 steel and PH13-8Mo steel exhibit body centered tetragonal martensitic matrix,  $D_{interstitial}$  in the steels could be similar [53]. In addition, previous studies reveal that dislocation density in the martensitic phase at room temperature is about  $4 \times 10^{15}$  per m<sup>2</sup> [54]. Similar dislocation density in martensitic steels is also reported by Shi et al. [55] and HajyAkbari et al. [56]. The microstructure of both steels is composed of martensitic matrix. Hence, the values of  $D_{interstitial}$  and  $D_{dislocations}$  for both steels can be supposed to be approximately equivalent, namely:

$$D_{interstitial}(PH17-4) + D_{dislocations}(PH17-4) \approx D_{interstitial}(PH13-8) + D_{dislocations}(PH13-8) \tag{12}$$

Subtracting Eq. (10) from Eq. (9), it can be expressed as:

$$D_{app}(PH17-4) - D_{app}(PH13-8) = [(D_{interstitial}(PH17-4) + D_{dislocations}(PH17-4)) - (D_{interstitial}(PH13-8) + D_{dislocations}(PH13-8))] + (D_{lath\ boundaries}(PH17-4) + D_{grain\ boundaries}(PH17-4)) - (D_{lath\ boundaries}(PH13-8) + D_{grain\ boundaries}(PH13-8)) + (D_{precipitates}(PH17-4) - D_{precipitates}(PH13-8)) \tag{11}$$

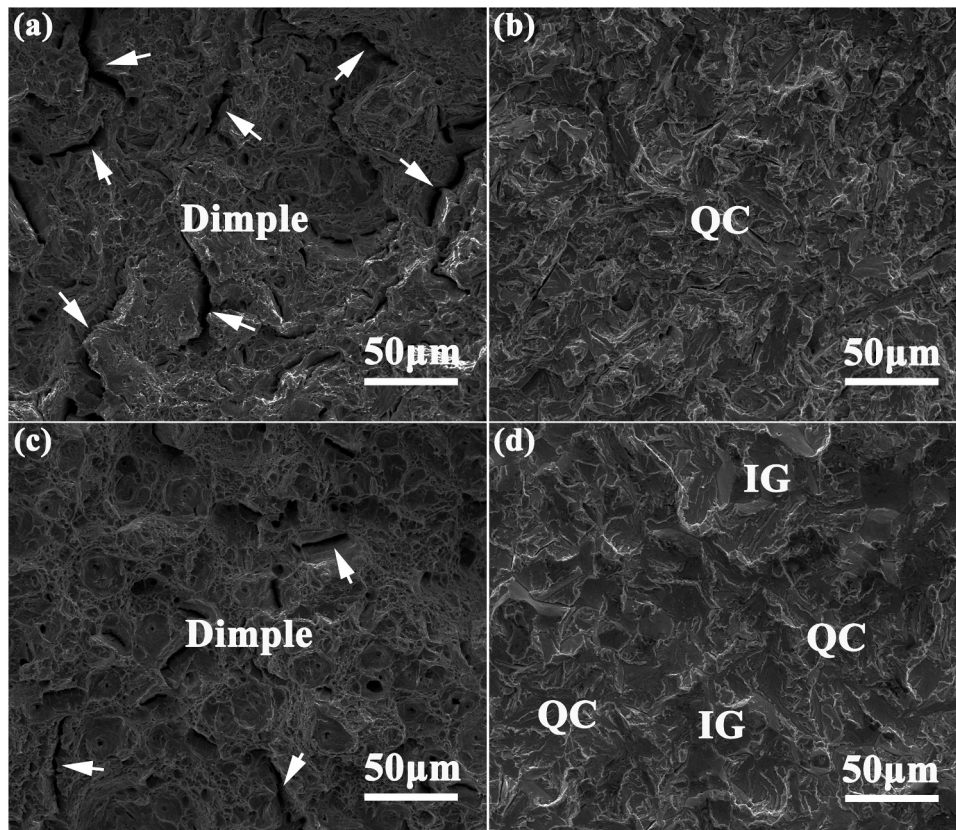


**Fig. 10.** Fracture surface images (a) HF and (b) HC PH17-4 steel; (c) HF and (d) HC PH13-8Mo steel. White arrows indicating secondary cracks. QC: quasi-cleavage. IG: intergranular fracture.

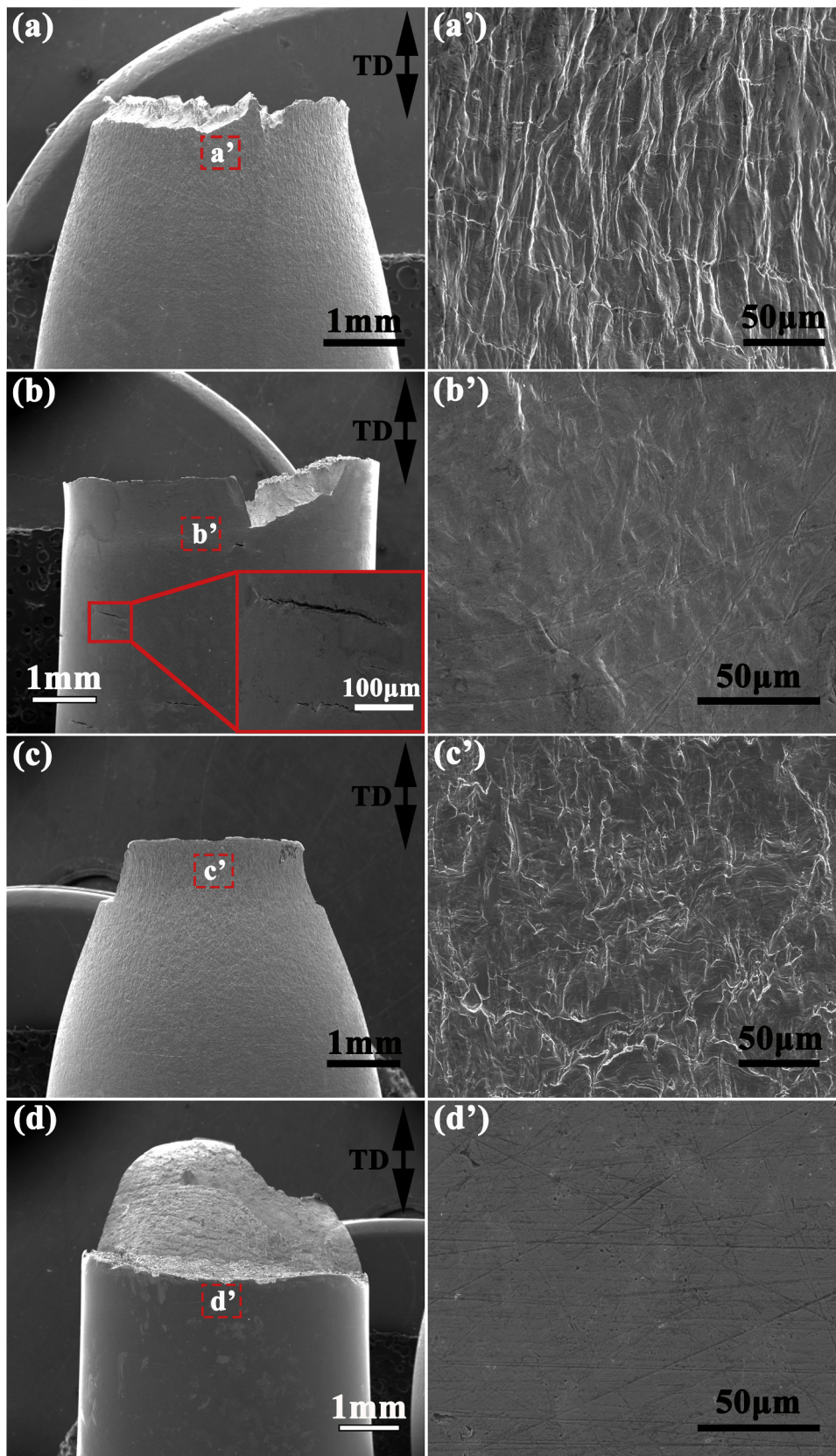


Fig. 11. Lateral side images of fractured samples (a) HF and (b) HC PH17-4 steel; (c) HF and (d) HC PH13-8Mo steel. (a')-(d') corresponding high magnification images of signified region in Fig. 11(a)-(d). TD: tensile direction.

Inserting Eq. (12) into Eq. (11), we can obtain:

$$D_{app(PH17-4)} - D_{app(PH13-8)} = [(D_{lath\ boundaries(PH17-4)} + D_{grain\ boundaries(PH17-4)}) - (D_{lath\ boundaries(PH13-8)} + D_{grain\ boundaries(PH13-8)})] + (D_{precipitates(PH17-4)} - D_{precipitates(PH13-8)}) \quad (13)$$

Compared with PH13-8Mo steel, PH17-4 steel possesses larger average grain size and lath size (Fig. 7), which indicates that less grain boundary and lath boundary hydrogen trapping sites are generated in PH17-4 steel at the same volume. It is reported that grain boundaries [57,58] and low angle lath boundaries [59] play dominant role in retardation hydrogen transport due to their trapping effect. Therefore, low grain boundary and lath boundary hydrogen trapping sites in PH17-4 steel correspond to high hydrogen diffusion coefficient, which can be written as:

$$D_{lath\ boundaries(PH17-4)} + D_{grain\ boundaries(PH17-4)} > D_{lath\ boundaries(PH13-8)} + D_{grain\ boundaries(PH13-8)} \quad (14)$$

Based on hydrogen permeation test results (Table 3), it can be obtained:

$$D_{app(PH17-4)} < D_{app(PH13-8)} \quad (15)$$

Combining Eqs. (13)–(15), we can obtain:

$$D_{precipitates(PH17-4)} < D_{precipitates(PH13-8)} \quad (16)$$

The Eq. (16) implies that the degree of obstructing hydrogen diffusion due to incoherent Cu-rich precipitates in PH17-4 steel is higher than that of coherent NiAl precipitates in PH13-8Mo steel, which is similar to results from Wei et al. [60] and Takahashi et al. [61], who reported that incoherent TiC and  $V_4C_3$  precipitates act as more effective hydrogen traps compared with coherent TiC and  $V_4C_3$  precipitates. This result can be explained from two aspects. On the one hand, incoherent precipitates arrest more hydrogen atoms compared with coherent precipitates. A study [60] indicates that the amount of hydrogen kept in incoherent precipitates mainly relies on their volume, because hydrogen atoms are dissolved inside these precipitates. The Cu-rich precipitates exhibit FCC structure and the radii of octahedral in FCC-Cu is calculated to be 0.0529 nm on the basis of the rigid-sphere model, which is twice as large as the radii of octahedral for NiAl BCC crystal (0.0206 nm). Moreover, incoherent interfaces between martensitic matrix and precipitates in steels also serve as additional hydrogen trapping sites [62], whereas coherent interfaces between martensitic matrix and precipitates of the steels can trap limited hydrogen atoms. Further, it is reported that both the core of misfit dislocations and less distorted location near misfit dislocations of coherent precipitates are considered as weak hydrogen trapping sites [35,63], and no hydrogen atoms are detected at small coherent precipitates [61]. On the other hand, activation energy of de-trapping hydrogen from incoherent precipitates is larger than that of coherent precipitates. With an increase in coherency of precipitates with ferrite matrix, hydrogen trapping activation energy decreases [60,63–65]. Wei et al. [60] reported that the activation energy for hydrogen desorption from coherent interfaces between the matrix and TiC precipitates was  $55.8 \text{ kJ mol}^{-1}$ , whereas it increased to  $68 \text{ kJ mol}^{-1}$ – $137 \text{ kJ mol}^{-1}$  for incoherent TiC interfaces.

**Table 4**

The related parameters used in the study to qualify precipitates strengthening and lath strengthening.

	$K_L$ (MPa $\mu\text{m}$ )	$\bar{L}$ (nm)	G (GPa)	b (nm)	$f$	$X$ (nm)
PH17-4	115 [73]	250	72 [75]	0.248 [74]	$1.54 \times 10^{-2}$ [54]	3.84
PH13-8Mo	115 [73]	212	72 [75]	0.248 [74]	$1.70 \times 10^{-2}$ [34]	3.25

The value of  $\bar{L}$  and  $X$  are derived from present study.

Lee et al. [65] also indicated that incoherent TiC had a larger trap activation energy of hydrogen than that of coherent ones, and as incoherent TiC precipitate sizes increased, corresponding activation energy of hydrogen desorption increased. Similarly, incoherent Cu-rich precipitates in PH17-4 steel have higher capability to trap hydrogen atoms and higher trap activation energy of de-trapping hydrogen in comparison with those of coherent NiAl precipitates in PH13-8Mo steel. Thus, relatively low apparent hydrogen diffusion coefficient and high apparent hydrogen solubility can be achieved in PH17-4 steel.

#### 4.2. Hydrogen embrittlement susceptibility of PH17-4 steel and PH13-8Mo steel

The susceptibility to HE of steels depends on the microstructures, such as grain sizes, lath sizes and precipitates. Previous studies [31,66–69] have demonstrated that fine grains or laths are beneficial to reducing HE sensibility and two possible explanations have been put forward. Firstly, as mentioned above, grain boundaries and lath boundaries act as hydrogen trapping sites. At the same volume, increasing grain/lath boundary trapping sites are achieved through grain and lath refinement. These hydrogen traps would hinder hydrogen accumulation at the crack tips through maintaining a uniform hydrogen distribution profile in the alloys, leading to high resistance to HE [67,69]. Secondly, coarse grains of steels are favorable for the nucleation of deformation twins in comparison with fine grains. Then high stress concentration region as well as preferential sites for hydrogen segregation is generated at the interactions of twin lamellas, causing premature cracking within coarse grains [31]. However, the present study result is controversial with previous experimental results [68,69], i.e., PH17-4 steel shows higher resistance to HE than that of PH13-8Mo steel, although average grain size and lath size of PH17-4 steel are larger than those of PH13-8Mo steel. For this case, we can deduce that the difference of precipitates is responsible for this abnormal phenomenon. Generally speaking, nano-sized precipitates of steels are beneficial to increasing the resistance to HE because they act as effective hydrogen trapping sites [70–72]. Unfortunately, no further analysis has been conducted to investigate whether these precipitates are coherent with the matrix in the previous studies [51,70,71]. It is worth mentioning that PH13-8Mo steel containing coherent NiAl precipitates exhibit higher HE susceptibility than PH17-4 steel with incoherent Cu-rich precipitates in the present study. As discussed in Section 4.1, incoherent Cu-rich precipitates in PH17-4 steel can capture hydrogen atoms efficiently and then reduce hydrogen diffusion behavior, which impedes hydrogen diffusion towards the specific region, such as the crack tip or potential failure sites, and result in high resistance to HE in PH17-4 steel. Moreover, for steels with primarily martensitic microstructure, yield strength ( $\sigma_y$ ) is contributed from lath boundary strengthening ( $\sigma_L$ ) and precipitate strengthening ( $\sigma_p$ ) and the other strengthening from solid solution strengthening and dislocation

**Table 5**

The respective contribution of lath boundary strengthening, precipitate strengthening and the other factors to yield strength for PH17-4 steel and PH13-8Mo steel.

	$\sigma_L$ (MPa)	$\sigma_P$ (MPa)	$\sigma_{Others}$ (MPa)
PH17-4	460	690	143
PH13-8Mo	542	722	171

strengthening ( $\sigma_{Others}$ ), which is expressed as [73]:

$$\sigma_y = \sigma_L + \sigma_P + \sigma_{Others} \quad (17)$$

The lath strengthening  $\sigma_L$  in Eq. (17) can be estimated by [73]:

$$\sigma_L = \frac{K_L}{\bar{L}} \quad (18)$$

where  $K_L$  represents the coefficient due to lath size (115 MPa  $\mu\text{m}$ ) [73] and  $\bar{L}$  is the average lath size ( $\mu\text{m}$ ). And the precipitation strengthening  $\sigma_P$  is estimated by the Ashby-Orowan relationship [74]:

$$\sigma_P = \left( \frac{0.538Gb\sqrt{f}}{X} \right) \ln \left( \frac{X}{2b} \right) \quad (19)$$

where  $G$  is shear modulus of Fe (72 GPa) [75],  $b$  is burgers vector (0.248 nm) [74],  $f$  is the volume fraction of precipitates and  $X$  is the diameter of the precipitates. Inserting related parameters (Table 4) to Eq. (18) and Eq. (19), yield strength increment from lath boundary strengthening, precipitate strengthening and other strengthening can be calculated, as summarized in Table 5. It can be seen that strengthening mechanism of PH17-4 and PH13-8Mo steel is dominated by precipitate strengthening, followed by lath strengthening and then other strengthening. In comparison with PH17-4 steel, the contribution from precipitate strengthening and lath strengthening to yield strength increment of PH13-8Mo steel is higher, resulting in higher strength of PH13-8Mo steel. According to results from previous studies [2,21,76,77], high strength level of the steels is one of reasons for their high HE sensibility. For example, Hui et al. [76] indicated that the susceptibility to HE of bainitic steel was much higher than that of pearlitic steel, which was mainly ascribed to higher strength level and microstructural characteristics of bainitic steel. A study [77] reported that cold drawing significantly increased the susceptibility to HE, which was mainly attributed to the combined effect of an increase of strength level, an increase of diffusible hydrogen absorption in the deformed materials and the occurrence of strain-induced martensite. Similarly, higher strength level of PH13-8Mo steel is responsible for its lower resistance to HE compared with PH17-4 steel.

## 5. Conclusion

- 1) The microstructure of PH17-4 steel and PH13-8Mo steel consists of lath martensite with fine precipitates. The average prior austenite grain size and lath spacing are 27  $\mu\text{m}$  and 250 nm for PH17-4 steel, and 23  $\mu\text{m}$  and 212 nm for PH13-8Mo steel, respectively. The incoherent Cu-rich precipitates with an average diameter of 3.84 nm are observed in PH17-4 steel, while PH13-8Mo steel exhibits coherent NiAl precipitates with an average size of 3.25 nm.
- 2) In comparison with PH17-4 steel, PH13-8Mo steel has superior strength, i.e., 1435 MPa and 1495 MPa vs 1293 MPa and 1430 MPa for yield strength and tensile strength respectively. The precipitate strengthening is dominant for both steels, followed by lath strengthening and then other strengthening.
- 3) Hydrogen permeation test results reveal that PH13-8Mo steel presents higher apparent hydrogen diffusion coefficient and lower apparent hydrogen solubility in comparison with those of PH17-4 steel. This is ascribed to the fact that incoherent Cu-rich precipitates in PH17-4 steel have higher capacity to trap hydrogen atoms

compared with coherent NiAl precipitates in PH13-8Mo steel.

- 4) PH13-8Mo steel exhibits higher HE sensibility than that of PH17-4 steel, which is mainly attributed to higher hydrogen diffusion behaviors and higher strength level of PH13-8Mo steel.

## Acknowledgement

The authors appreciate T Wang in Dongfang Turbine Co., Ltd. for providing experimental materials. The authors acknowledge the help of N Zou in Washington State University for collecting some SEM images.

## References

- [1] C.N. Hsiao, C.S. Chiou, J.R. Yang, Aging reactions in a 17-4 PH stainless steel, *Mater. Chem. Phys.* 74 (2002) 134–142.
- [2] X. Li, J. Zhang, E. Akiyama, Q. Li, Y. Wang, Effect of heat treatment on hydrogen-assisted fracture behavior of PH13-8Mo steel, *Corros. Sci.* 128 (2017) 198–212.
- [3] D. Susan, T. Crenshaw, J. Gearhart, The effects of casting porosity on the tensile behavior of investment cast 17-4PH stainless steel, *J. Mater. Eng. Perform.* 24 (2015) 2917–2924.
- [4] R. Schnitzer, R. Radis, M. Nöhner, M. Schober, R. Hochfellner, S. Zinner, et al., Reverted austenite in PH 13-8 Mo maraging steels, *Mater. Chem. Phys.* 122 (2010) 138–145.
- [5] X. Li, J. Zhang, Y. Wang, S. Shen, X. Song, Effect of hydrogen on tensile properties and fracture behavior of PH 13-8 Mo steel, *Mater. Des.* 108 (2016) 608–617.
- [6] S.A. Razavi, F. Ashrafizadeh, S. Fooladi, Prediction of age hardening parameters for 17-4PH stainless steel by artificial neural network and genetic algorithm, *Mater. Sci. Eng.: A* 675 (2016) 147–152.
- [7] W. Maktouf, K. Sai, An investigation of premature fatigue failures of gas turbine blade, *Eng. Fail. Anal.* 47 (2015) 89–101.
- [8] R. Dewangan, J. Patel, J. Dubey, P.K. Sen, S.K. Bohidar, Gas turbines blades—a critical review of failure on first and second stages, *Int. J. Mech. Eng. Robot. Res.* 4 (2015) 216.
- [9] T. Zuo, Study on Fatigue Behaviors of Steel 2Cr12NiW1Mo1V for Turbine Blade (Thesis), Xi'an Jiaotong University, 2013.
- [10] G. Das, S. Ghosh Chowdhury, A. Kumar Ray, S. Kumar Das, D. Kumar Bhattacharya, Turbine blade failure in a thermal power plant, *Eng. Fail. Anal.* 10 (2003) 85–91.
- [11] R. Ebara, Corrosion fatigue phenomena learned from failure analysis, *Eng. Fail. Anal.* 13 (2006) 516–525.
- [12] R. Ebara, Corrosion fatigue crack initiation in 12% chromium stainless steel, *Mater. Sci. Eng.: A* 468 (2007) 109–113.
- [13] Y.-j. Xie, M.-c. Wang, G. Zhang, M. Chang, Analysis of superalloy turbine blade tip cracking during service, *Eng. Fail. Anal.* 13 (2006) 1429–1436.
- [14] A.P. Tschitschin, C.R.F. Azevedo, Failure analysis of turbo-blower blades, *Eng. Fail. Anal.* 12 (2005) 49–59.
- [15] W.-Z. Wang, F.-Z. Xuan, K.-L. Zhu, S.-T. Tu, Failure analysis of the final stage blade in steam turbine, *Eng. Fail. Anal.* 14 (2007) 632–641.
- [16] B. Syrett, R. Viswanathan, S. Wing, J. Wittig, Effect of microstructure on pitting and corrosion fatigue of 17-4 PH turbine blade steel in chloride environments, *Corrosion* 38 (1982) 273–282.
- [17] H. Kim, Crack evaluation of the fourth stage blade in a low-pressure steam turbine, *Eng. Fail. Anal.* 18 (2011) 907–913.
- [18] L.K. Bhagi, P. Gupta, V. Rastogi, Fractographic investigations of the failure of L-1 low pressure steam turbine blade. case studies in, *Eng. Fail. Anal.* 1 (2013) 72–78.
- [19] J. Yao, C. Dong, C. Man, K. Xiao, X. Li, The electrochemical behavior and characteristics of passive film on 2205 duplex stainless steel under various hydrogen charging conditions, *Corrosion* 72 (2015) 42–50.
- [20] X. Li, J. Zhang, Y. Wang, M. Ma, S. Shen, X. Song, The dual role of shot peening in hydrogen-assisted cracking of PSB1080 high strength steel, *Mater. Des.* 110 (2016) 602–615.
- [21] X. Li, J. Zhang, Q. Fu, X. Song, S. Shen, Q. Li, A comparative study of hydrogen embrittlement of 20SiMn2CrNiMo, PSB1080 and PH13-8Mo high strength steels, *Mater. Sci. Eng.: A* (2018).
- [22] S. Shen, X. Li, P. Zhang, Y. Nan, G. Yang, X. Song, Effect of solution-treated temperature on hydrogen embrittlement of 17-4 PH stainless steel, *Mater. Sci. Eng.: A* 703 (2017) 413–421.
- [23] L. Wu, Y. Takeda, T. Shoji, M. Yamashita, S. Izumi, The influence of tempering treatment on the microstructure evolution and corrosion resistance of precipitation hardening 17-4 stainless steel, *Corrosion* 72 (2016) 1083–1094.
- [24] S. Tavares, C. Machado, I. Oliveira, T. Martins, M. Masoumi, Damage associated with the interaction between hydrogen and microstructure in a high sulfur 17-4PH steel for studs, *Eng. Fail. Anal.* 82 (2017) 642–647.
- [25] Coseglio MSDR, Sulphide stress cracking of 17-4 PH for applications in oilfield components, *Mater. Sci. Technol.* 33 (2017) 1863–1878.
- [26] X. Li, J. Zhang, J. Chen, S. Shen, G. Yang, T. Wang, et al., Effect of aging treatment on hydrogen embrittlement of PH 13-8 Mo martensite stainless steel, *Mater. Sci. Eng.: A* 651 (2016) 474–485.
- [27] Y. Ding, L. Tsay, M. Chiang, C. Chen, Gaseous hydrogen embrittlement of PH 13-8 Mo steel, *J. Nucl. Mater.* 385 (2009) 538–544.
- [28] L. Tsay, M. Chi, H. Chen, C. Chen, Investigation of hydrogen sulfide stress corrosion cracking of PH 13-8 Mo stainless steel, *Mater. Sci. Eng.: A* 416 (2006) 155–160.
- [29] E. Akiyama, S. Li Electrochemical Hydrogen Permeation Tests Under Potentiostatic

- Hydrogen Charging Conditions Conventionally Used for Hydrogen Embrittlement Study. Meeting Abstracts: The Electrochemical Society. p. 1302.
- [30] X. Li, J. Zhang, M. Ma, X. Song, Effect of shot peening on hydrogen embrittlement of high strength steel, *Int. J. Miner. Metall. Mater.* 23 (2016) 667–675.
- [31] N. Zan, H. Ding, X. Guo, Z. Tang, W. Bleck, Effects of grain size on hydrogen embrittlement in a Fe-22Mn-0.6C TWIP steel, *Int. J. Hydrog. Energy* 40 (2015) 10687–10696.
- [32] X. Li, J. Zhang, Q. Fu, E. Akiyama, X. Song, Y. Wang, et al., Tensile mechanical properties and fracture behaviors of nickel-based superalloy 718 in the presence of hydrogen, *Int. J. Hydrog. Energy* (2018).
- [33] S. Frappart, X. Feaugas, J. Creus, F. Thebault, L. Delattre, H. Marchebois, Study of the hydrogen diffusion and segregation into Fe–C–Mo martensitic HSLA steel using electrochemical permeation test, *J. Phys. Chem. Solids* 71 (2010) 1467–1479.
- [34] C. Hsiao, C. Chiou, J. Yang, Aging reactions in a 17-4 PH stainless steel, *Mater. Chem. Phys.* 74 (2002) 134–142.
- [35] L.W. Tsay, H.H. Chen, M.F. Chiang, C. Chen, The influence of aging treatments on sulfide stress corrosion cracking of PH 13-8 Mo steel welds, *Corros. Sci.* 49 (2007) 2461–2473.
- [36] C. Chi, H. Yu, J. Dong, W. Liu, S. Cheng, Z. Liu, et al., The precipitation strengthening behavior of Cu-rich phase in Nb contained advanced Fe–Cr–Ni type austenitic heat resistant steel for USC power plant application, *Prog. Nat. Sci.: Mater. Int.* 22 (2012) 175–185.
- [37] K. Hirano, M. Cohen, B. Averbach, Diffusion of nickel into iron, *Acta Metall.* 9 (1961) 440–445.
- [38] J. Hirvonen, J. Räsänen, Diffusion of aluminum in ion-implanted alpha iron, *J. Appl. Phys.* 53 (1982) 3314–3316.
- [39] G. Salje, M. Feller-Kniepmeier, The diffusion and solubility of copper in iron, *J. Appl. Phys.* 48 (1977) 1833–1839.
- [40] S. Jiang, H. Wang, Y. Wu, X. Liu, H. Chen, M. Yao, et al., Ultrastrong steel via minimal lattice misfit and high-density nanoprecipitation, *Nature* 544 (2017) 460.
- [41] X. Li, J. Zhang, D. Hou, Q. Li, Compressive deformation and fracture behaviors of AZ31 magnesium alloys with equiaxed grains and bimodal grains, *Mater. Sci. Eng.: A* (2018).
- [42] S.-J. Lee, J.A. Ronevich, G. Krauss, D.K. Matlock, Hydrogen embrittlement of hardened low-carbon sheet steel, *ISIJ Int.* 50 (2010) 294–301.
- [43] Y. Takeda, C. McMahon, Strain controlled vs stress controlled hydrogen induced fracture in a quenched and tempered steel, *Metall. Trans. A* 12 (1981) 1255–1266.
- [44] F. Rehr, K. Mraczek, A. Pichler, E. Werner, Mechanical properties and fracture behavior of hydrogen charged AHSS/UHSS grades at high-and low strain rate tests, *Mater. Sci. Eng.: A* 590 (2014) 360–367.
- [45] F. Nakasato, I. Bernstein, Crystallographic and fractographic studies of hydrogen-induced cracking in purified iron and iron-silicon alloys, *Metall. Trans. A* 9 (1978) 1317–1326.
- [46] X. Li, J. Zhang, E. Akiyama, Y. Wang, Q. Li, Microstructural and crystallographic study of hydrogen-assisted cracking in high strength PSB1080 steel, *Int. J. Hydrog. Energy* (2018).
- [47] X. Li, J. Zhang, Y. Wang, B. Li, P. Zhang, X. Song, Effect of cathodic hydrogen-charging current density on mechanical properties of prestrained high strength steels, *Mater. Sci. Eng.: A* 641 (2015) 45–53.
- [48] N. Winzer, O. Rott, R. Thiessen, I. Thomas, K. Mraczek, T. Höche, et al., Hydrogen diffusion and trapping in Ti-modified advanced high strength steels, *Mater. Des.* 92 (2016) 450–461.
- [49] H.K.D.H. Bhadeshia, Prevention of hydrogen embrittlement in steels, *ISIJ Int.* 56 (2016) 24–36.
- [50] M. Koyama, C.C. Tasan, E. Akiyama, K. Tsuzaki, D. Raabe, Hydrogen-assisted decohesion and localized plasticity in dual-phase steel, *Acta Mater.* 70 (2014) 174–187.
- [51] X. Shi, W. Yan, W. Wang, Y. Shan, K. Yang, Novel Cu-bearing high-strength pipeline steels with excellent resistance to hydrogen-induced cracking, *Mater. Des.* 92 (2016) 300–305.
- [52] M. Khedr, W. Li, X. Zhu, P. Zhou, S. Gao, X. Jin, Improving hydrogen embrittlement resistance of Hadfield steel by thermo-mechanical flash-treatment, *Mater. Sci. Eng.: A* 712 (2018) 133–139.
- [53] K. Kiuchi, R. McLellan, The Solubility and Diffusivity of Hydrogen in Well-annealed ad Deformed Iron. Perspectives in Hydrogen in Metals, Elsevier, 1986, pp. 29–52.
- [54] K.H. Matlack, H.A. Bradley, S. Thiele, J.-Y. Kim, J.J. Wall, H.J. Jung, et al., Nonlinear ultrasonic characterization of precipitation in 17-4PH stainless steel, *NDT & E Int.* 71 (2015) 8–15.
- [55] Z. Shi, W. Gong, Y. Tomota, S. Harjo, J. Li, B. Chi, et al., Study of tempering behavior of lath martensite using in situ neutron diffraction, *Mater. Charact.* 107 (2015) 29–32.
- [56] F. HajyAkbari, J. Sietsma, A.J. Böttger, M.J. Santofimia, An improved X-ray diffraction analysis method to characterize dislocation density in lath martensitic structures, *Mater. Sci. Eng.: A* 639 (2015) 208–218.
- [57] J. Yao, J. Cahoon, Experimental studies of grain boundary diffusion of hydrogen in metals, *Acta Metall. Mater.* 39 (1991) 119–126.
- [58] S. Taketomi, R. Matsumoto, N. Miyazaki, Atomistic study of hydrogen distribution and diffusion around a {112} < 111 > edge dislocation in alpha iron, *Acta Mater.* 56 (2008) 3761–3769.
- [59] A. Oudriss, J. Creus, J. Bouhattate, E. Conforto, C. Berziou, C. Savall, et al., Grain size and grain-boundary effects on diffusion and trapping of hydrogen in pure nickel, *Acta Mater.* 60 (2012) 6814–6828.
- [60] F.-G. Wei, K. Tsuzaki, Quantitative analysis on hydrogen trapping of TiC particles in steel, *Metall. Mater. Trans. A* 37 (2006) 331–353.
- [61] J. Takahashi, K. Kawakami, T. Tarui, Direct observation of hydrogen-trapping sites in vanadium carbide precipitation steel by atom probe tomography, *Scr. Mater.* 67 (2012) 213–216.
- [62] T. Depover, D.P. Escobar, E. Wallaert, Z. Zermout, K. Verbeken, Effect of hydrogen charging on the mechanical properties of advanced high strength steels, *Int. J. Hydrog. Energy* 39 (2014) 4647–4656.
- [63] F. Wei, K. Tsuzaki, Hydrogen absorption of incoherent TiC particles in iron from environment at high temperatures, *Metall. Mater. Trans. A* 35 (2004) 3155–3163.
- [64] K. Kawakami, T. Matsumiya, Numerical analysis of hydrogen trap state by TiC and V4C3 in bcc-Fe, *ISIJ Int.* 52 (2012) 1693–1697.
- [65] S.M. Lee, J.Y. Lee, The effect of the interface character of TiC particles on hydrogen trapping in steel, *Acta Metall.* 35 (1987) 2695–2700.
- [66] C. Park, N. Kang, S. Liu, Effect of grain size on the resistance to hydrogen embrittlement of API 2W Grade 60 steels using in situ slow-strain-rate testing, *Corros. Sci.* 128 (2017) 33–41.
- [67] Y. Bai, Y. Tian, S. Gao, A. Shibata, N. Tsuji, Hydrogen embrittlement behaviors of ultrafine-grained 22Mn–0.6C austenitic twinning induced plasticity steel, *J. Mater. Res.* 32 (2017) 4592–4604.
- [68] I.-J. Park, S.-m. Lee, H.-h. Jeon, Y.-K. Lee, The advantage of grain refinement in the hydrogen embrittlement of Fe–18Mn–0.6C twinning-induced plasticity steel, *Corros. Sci.* 93 (2015) 63–69.
- [69] Y. Bai, Y. Momotani, M.C. Chen, A. Shibata, N. Tsuji, Effect of grain refinement on hydrogen embrittlement behaviors of high-Mn TWIP steel, *Mater. Sci. Eng.: A* 651 (2016) 935–944.
- [70] X. Zhu, W. Li, T. Hsu, S. Zhou, L. Wang, X. Jin, Improved resistance to hydrogen embrittlement in a high-strength steel by quenching–partitioning–tempering treatment, *Scr. Mater.* 97 (2015) 21–24.
- [71] A. Nagao, M.L. Martin, M. Dadfarnia, P. Sofronis, I.M. Robertson, The effect of nanosized (Ti, Mo) C precipitates on hydrogen embrittlement of tempered lath martensitic steel, *Acta Mater.* 74 (2014) 244–254.
- [72] H.-J. Kim, S.-H. Jeon, W.-S. Yang, B.-G. Yoo, Y.-D. Chung, H.-Y. Ha, et al., Effects of titanium content on hydrogen embrittlement susceptibility of hot-stamped boron steels, *J. Alloy. Compd.* 735 (2018) 2067–2080.
- [73] H. Bhadeshia, R. Honeycombe, *Steels: Microstructure and Properties*, Butterworth-Heinemann, 2017.
- [74] T. Gladman, Precipitation hardening in metals, *Metal. Sci. J.* 15 (1999) 30–36.
- [75] T. Gressmann, M. Wohlschlägel, S. Shang, U. Welzel, A. Leineweber, E. Mittemeijer, et al., Elastic anisotropy of  $\gamma'$ -Fe<sub>3</sub>N and elastic grain interaction in  $\gamma'$ -Fe<sub>3</sub>N<sub>1</sub> layers on  $\alpha$ -Fe: first-principles calculations and diffraction stress measurements, *Acta Mater.* 55 (2007) 5833–5843.
- [76] W. Hui, Z. Xu, Y. Zhang, X. Zhao, C. Shao, Y. Weng, Hydrogen embrittlement behavior of high strength rail steels: a comparison between pearlitic and bainitic microstructures, *Mater. Sci. Eng.: A* 704 (2017) 199–206.
- [77] W. Hui, Y. Zhang, X. Zhao, C. Shao, K. Wang, W. Sun, et al., Influence of cold deformation and annealing on hydrogen embrittlement of cold hardening bainitic steel for high strength bolts, *Mater. Sci. Eng.: A* 662 (2016) 528–536.